Lithium-Ion Batteries Hot Paper

Deutsche Ausgabe: DOI: 10.1002/ange.201705200
Internationale Ausgabe: DOI: 10.1002/anie.201705200

Colloidal Synthesis of Silicon–Carbon Composite Material for Lithium-Ion Batteries

Haiping Su, Alejandro A. Barragan, Linxiao Geng, Donghui Long, Licheng Ling, Krassimir N. Bozhilov, Lorenzo Mangolini, and Juchen Guo**

Abstract: *We report colloidal routes to synthesize silicon@-carbon composites for the first time. Surface-functionalized Si nanoparticles (SiNPs) dissolved in styrene and hexadecane are used as the dispersed phase in oil-in-water emulsions, from which yolk–shell and dual-shell hollow SiNPs@C composites are produced via polymerization and subsequent carbonization. As anode materials for Li-ion batteries, the SiNPs@C composites demonstrate excellent cycling stability and rate performance, which is ascribed to the uniform distribution of SiNPs within the carbon hosts. The Li-ion anodes composed of 46 wt % of dual-shell SiNPs@C, 46 wt % of graphite, 5 wt % of acetylene black, and 3 wt % of carboxymethyl cellulose with an areal loading higher than 3 mg cm^{-2} achieve an overall specific capacity higher than 600 mAh g^{-1}, which is an improvement of more than 100 % compared to the pure graphite anode. These new colloidal routes present a promising general method to produce viable Si–C composites for Li-ion batteries.*

Silicon is recognized as the most promising anode material to replace or complement graphite in lithium-ion (Li-ion) batteries.[1] However, the large volume change associated with lithiation/delithiation of Si causes significant challenges to practical Si-based anodes.[2] Although particle pulverization may no longer be the primary problem since the use of Si of nanosize or with nanofeatures,[3] repeated volume change can degrade the electrical contact and destabilize the solid electrolyte interphase (SEI) in the electrodes.[4] Therefore, composite materials with Si primary particles incorporated into secondary structures, particularly Si–C composites, are often investigated as a method to accommodate the impact of Si volume change.[5] For optimal Si–C composites, the Si particles are ideally small with narrow size distribution to minimize the absolute dimensional change.[6] The Si particles also need to be uniformly dispersed in the carbon structure to achieve homogeneous lithiation/delithiation.[7] In addition, certain porosity of the carbon framework is necessary to maintain the overall dimensional stability during lithiation/delithiation.[2a]

To date, Si–C composites with various nanostructures including yolk–shell Si–C,[2a,8] pomegranate-like Si–C,[6c] sandwich-structured Si–graphene oxide,[9] graphene or carbon coated silicon nanoparticles or nanowires[10] have demonstrated excellent electrochemical performance. Clearly, incorporating Si into a carbon matrix does indeed improve the structural and electrical integrity of the Si–C composites.[11] However, most of the synthetic methods in use still face challenges in the uniform dispersal of the primary Si particles due to their poor solubility in any solvent. Herein we report a unique colloidal method to synthesize Si@C composites using Si nanoparticles (SiNPs) that are soluble in organic solvents. Using a scalable non-thermal plasma synthetic method developed by the Mangolini group,[12] we synthesized SiNPs with hydrogen-terminated surface and an average particle size of approximately 5 nm with narrow size distribution (Figure S1 in the Supporting Information). Enabled by the surface −H, dodecyl chains ($-C_{12}H_{25}$) were tethered onto the SiNP surface upon reaction with dodecane. The obtained $C_{12}H_{25}$-SiNPs became readily soluble in many organic solvents. The Si content in $C_{12}H_{25}$-SiNPs is 86.5 wt % as measured with thermogravimetric analysis (TGA, Figure S2). To synthesize the SiNPs@C composite, $C_{12}H_{25}$-SiNPs were first dissolved in styrene, and the obtained solution was dispersed in the aqueous solution of hexadecyltrimethylammonium bromide by sonication to form a stable emulsion. Free radical emulsion polymerization was then initiated to produce a colloid of SiNPs@polystyrene (SiNPs@PS) particles dispersed in water. The SiNPs@PS particles were subsequently coated with a layer of resorcinol–formaldehyde resin (RF) via a seeded sol–gel synthesis followed by carbonization to produce the SiNPs@C composite denoted as SiNPs@C_{PS}.

The transmission electron microscopic (TEM) image, high-angle annular dark-field (HAADF) image, and the energy-dispersive X-ray spectroscopy (EDX) elemental mapping of the SiNPs@C_{PS} are shown in Figure 1. The TEM image

[*] H. Su, Prof. D. Long, Prof. L. Ling
State Key Laboratory of Chemical Engineering
East China University of Science and Technology
Meilong Rd, Shanghai, 200237 (P.R. China)
E-mail: longdh@mail.ecust.edu.cn

H. Su, L. Geng, Prof. J. Guo
Department of Chemical and Environmental Engineering
University of California, Riverside
900 University Ave, Riverside, CA 92521 (USA)
E-mail: jguo@engr.ucr.edu

A. A. Barragan, Prof. L. Mangolini
Department of Mechanical Engineering
University of California, Riverside (USA)

Dr. K. N. Bozhilov, Prof. L. Mangolini, Prof. J. Guo
Materials Science and Engineering Program
University of California, Riverside (USA)

Dr. K. N. Bozhilov
Central Facility for Advanced Microscopy and Microanalysis, University of California
Riverside (USA)

Supporting information and the ORCID identification number(s) for the author(s) of this article can be found under: https://doi.org/10.1002/anie.201705200.

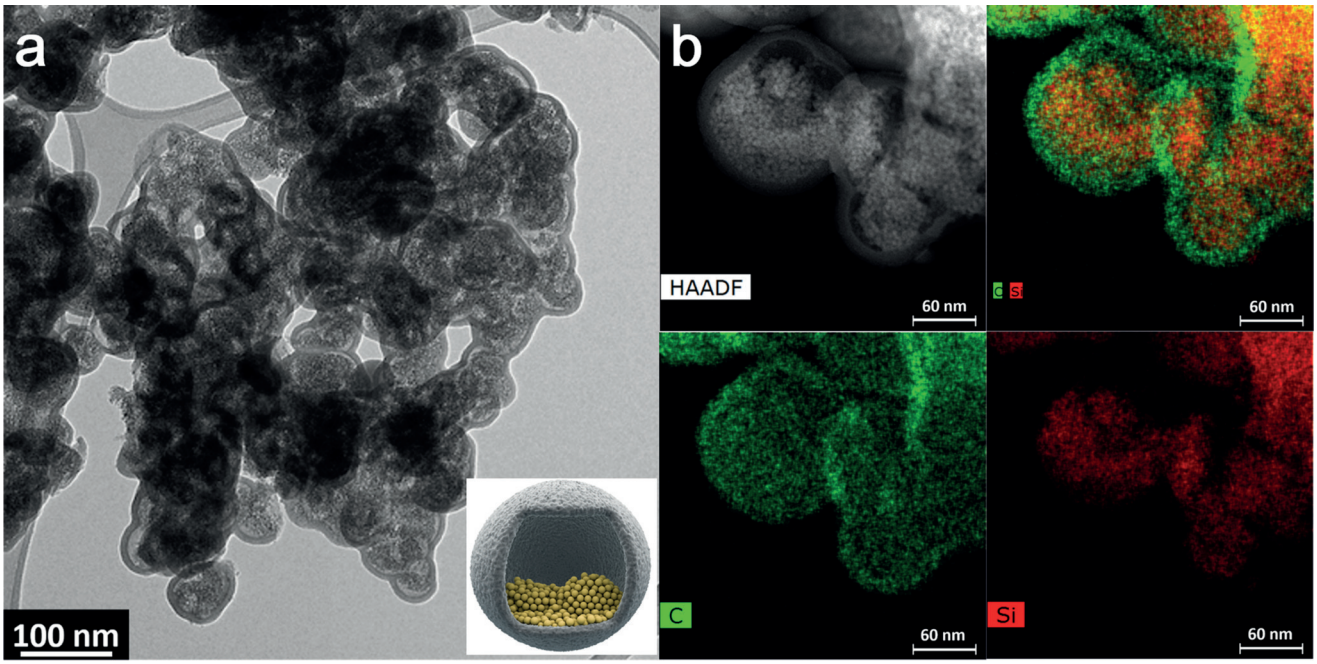

Figure 1. a) TEM image of the SiNPs@C_{PS} composite with schematic inset, b) dark field TEM image and EDX elemental mapping of the SiNPs@C_{PS} composite.

clearly shows the SiNPs were enclosed in thin (ca. 10 nm) carbon shells. The HAADF image and the elemental mapping reveal the yolk–shell structure of the individual SiNPs@C_{PS} particle, which is illustrated in the schematic inset. The yolk–shell structure originated from the formation of SiNPs@PS particles in the emulsion polymerization: The droplets of styrene became more viscous during polymerization while the solubility of $C_{12}H_{25}$-SiNPs in the droplets decreased, leading to phase separation (i.e. SiNPs aggregated and separated from PS). As a result, the synthesized SiNPs@PS particle attained the Janus morphology with clear separation of the SiNPs aggregation on one side of the particle (Figure S3). The PS portion of the Janus particles underwent decomposition during the carbonization of SiNPs@PS@RF, thus resulting in the yolk–shell SiNPs@C_{PS}. The specific surface area of the SiNPs@C_{PS} composite was 437 $m^2 g^{-1}$ with a specific pore volume of 0.45 $cm^3 g^{-1}$ from the N_2 adsorption–desorption isotherms analysis (Figure S4 and Table S1). To measure the Si content in SiNPs@C_{PS}, TGA of the composite was performed in dry air from room temperature to 800 °C at 10 °C min^{-1} to fully remove the carbon and oxidize Si to SiO_2. From the mass of the obtained SiO_2, the Si content in SiNPs@C_{PS} was calculated as 35 wt% (Figure S2 in the Supporting Information).

The Li-ion anode performance of the SiNPs@C_{PS} composite was evaluated in a half-cell configuration with Li as the counter electrode. Figure 2a shows the cycle stability and coulombic efficiency (CE) of SiNPs@C_{PS} at lithiation/delithiation rates of 1/10 C, 1/3 C, 1 C, and 2 C (1 C is defined as 1 Ag^{-1} with respect to the mass of SiNPs@C_{PS}, which is 85 wt% of the electrode). Despite the low initial CE (ICE) (43% at 1/10 C, 41% at 1/3 C, 30% at 1 C, and 30% at 2 C),

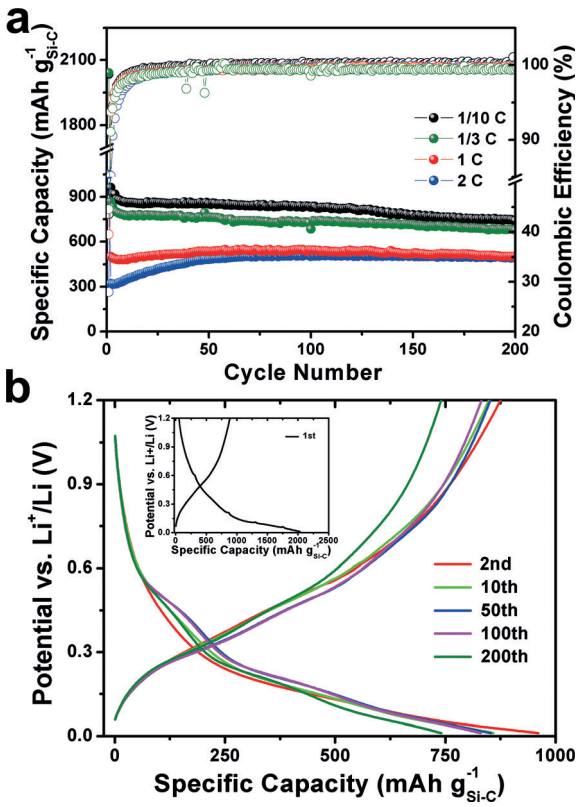

Figure 2. a) Cycle stability and CE of the SiNPs@C_{PS} composite at different C rate and b) representative lithiation/delithiation voltage profiles at 1/10 C vs. Li^+/Li. Inset is the voltage profile of the first cycle.

the reversible capacities were stabilized after the second cycle. After 200 cycles, the remaining lithiation capacities were 740 mAh g^{-1} at 1/10 C, 678 mAh g^{-1} at 1/3 C, 505 mAh g^{-1} at 1 C, and 502 mAh g^{-1} at 2 C, and the corresponding capacity retentions were 77% (vs. the 2nd cycle at 1/10 C), 78% (vs. the 2nd cycle at 1/3 C), 92% (vs. the highest capacity at 1 C), and 96% (vs. the highest capacity at 2 C). Figure 2b displays the representative lithiation/delithiation curves at 1/10 C, demonstrating a stable potential profile. The cycle stability of the electrodes composed of SiNPs@C_{PS} is significantly improved from those composed of pure SiNPs with the same weight ratio (Figure S5), which can be attributed to the yolk–shell structure accommodating the volume change of Si. However, the ICE is low, likely due to the SEI formation promoted by the relatively high specific surface area and the hydroxy surface groups residue from the RF carbon precursor.[4c,13] The Si content is limited by the solubility of $C_{12}H_{25}$-SiNPs in styrene. Furthermore, the aggregation of SiNPs inside the carbon shell is not the ideal particle distribution, which could be responsible for the capacity fading during the cycling.

To improve the performance of the SiNPs@C composite, a modified colloidal method was developed. Instead of styrene, hexadecane (HD) was used to dissolve $C_{12}H_{25}$-SiNPs and as the dispersed phase in the oil-in-water emulsion. Resorcinol and formaldehyde were subsequently dissolved into the emulsion, followed by adding ammonium hydroxide to initiate the sol–gel formation of RF on the surface of the droplets of the $C_{12}H_{25}$-SiNPs solution in HD. The synthesized SiNPs-in-HD@RF particles were extracted and carbonized to produce the SiNPs@C composite denoted as SiNPs@C_{HD}. The TEM image in Figure 3a shows the microstructure of SiNPs@C_{HD} composed of fused hollow carbon spheres encapsulating SiNPs. The HAADF image and the elemental mapping in Figure 3b reveal the dual-shell hollow structure of the individual SiNPs@C_{HD} particle with SiNPs uniformly coated on the inner wall of the carbon shell (illustrated in the inset of Figure 3a), which is clearly different from the yolk–shell structure of SiNPs@C_{PS}. The formation of the dual-shell hollow structure is attributed to the use of SiNPs-in-HD droplets as the template for RF coating in the colloidal synthesis: each droplet remained as a homogenous solution of SiNPs without aggregation during the sol–gel RF coating process. Upon evaporation of HD, SiNPs were uniformly coated on the inner wall of the RF shell, which retained its structure after carbonization. The TEM images of the SiNPs@RF particles before carbonization and SiNPs@C_{HD} at high magnification are shown in Figures S6 and 7.

Not only is the morphology improved by the modified route, but the specific surface area and pore volume of SiNPs@C_{HD} are also reduced to 317 m^2 g^{-1} and 0.23 cm^3 g^{-1} (Figure S4 and Table S1). Furthermore, the Si content is enhanced to 46 wt% due to the higher solubility and stability of $C_{12}H_{25}$-SiNPs in HD (Figure S2). The electrochemical performance of the SiNPs@C_{HD} composite was evaluated under the same conditions as those used to test SiNPs@C_{PS}. Figure 4 shows the unambiguously improved performance of SiNPs@C_{HD} compared to SiNPs@C_{PS} in parameters including capacity, CE, and cycle stability. The ICE is 49% at 1/10 C, 47% at 1/3 C, 44% at 1 C, and 36% at 2 C. Although these ICEs are still modest, it is a considerable improvement from those of SiNPs@C_{PS}. The CE of SiNPs@C_{HD} during prolonged cycling is also improved from that of SiNPs@C_{PS}. The lithiation capacity at the second cycle are 1074 mAh g^{-1} at 1/10 C, 786 mAh g^{-1} at 1/3 C, 410 mAh g^{-1} at 1 C, and 385 mAh g^{-1} at 2 C, which are all higher than those of SiNPs@C_{PS}. Finally, the capacity retention is significantly improved: the remaining lithiation capacities after 200 cycles

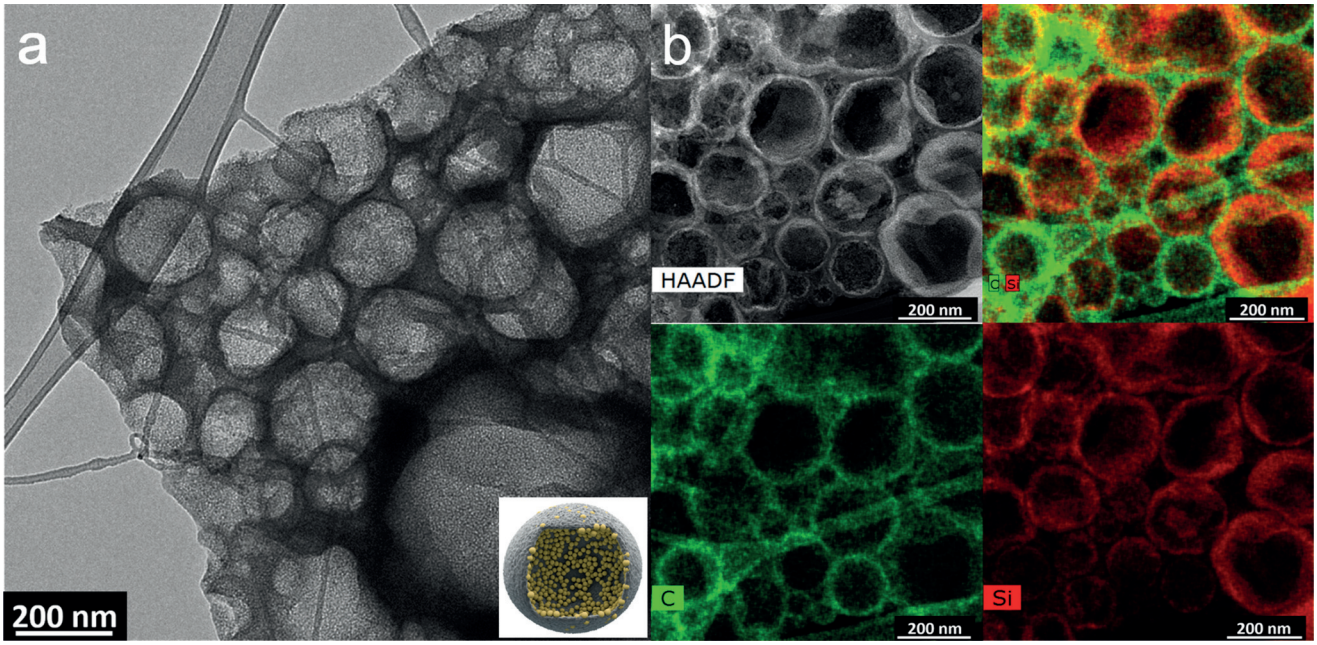

Figure 3. a) TEM image of the SiNPs@C_{HD} composite with schematic inset, b) dark field TEM image and EDX elemental mapping of the SiNPs@C_{HD} composite.

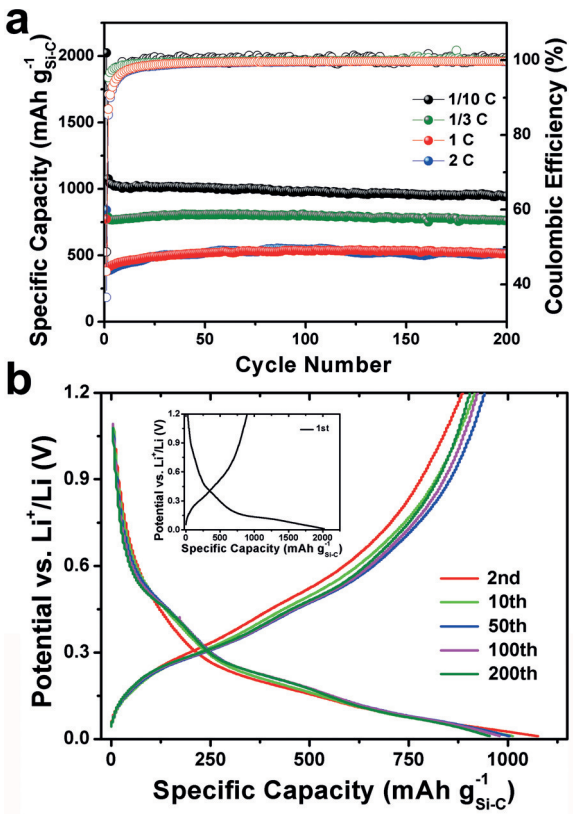

Figure 4. a) Cycle stability and CE of the SiNPs@C_{HD} composite at different C rates and b) representative lithiation/delithiation voltage profiles at 1/10 C vs. Li^+/Li. Inset is the voltage profile of the first cycle.

are 980 mAh g^{-1} at 1/10 C, 763 mAh g^{-1} at 1/3 C, 512 mAh g^{-1} at 1 C, and 511 mAh g^{-1} at 2 C, corresponding to 92 % (vs. the 2nd cycle at 1/10 C), 97 % (vs. the 2nd cycle at 1/3 C), 95 % (vs. the highest capacity at 1 C) and 93 % (vs. the highest capacity at 2 C) retentions. The TEM analysis of the SiNPs@C_{HD} composite after 200 cycles at 1/3 C indicates the integrity of the dual-shell microstructure is intact (Figure S8).

The most realistic application of Si-based composites is their use as additives to conventional graphite anodes to boost their capacities.[14] Therefore, the SiNPs@C_{HD} composite was further evaluated in an electrode composed of 46 wt % of SiNPs@C_{HD}, 46 wt % of commercial graphite, 5 wt % of acetylene black, and 3 % of carboxymethyl cellulose binder, with a mass loading of the active materials (SiNPs@C_{HD} + graphite) higher than 3 mg cm^{-2}. A disadvantage of the SiNPs@C_{HD} composite is its low ICE which can be attributed to the high surface area and the hydroxy surface groups residue from the RF carbon precursor to promote SEI formation. Previous studies have demonstrated that carbon coating via chemical vapor deposition (CVD) on Si electrodes can effectively improve the ICE of Si-based anodes.[15] The high purity of carbon produced from CVD methods can stabilize the SEI formation and eliminate the undesirable surface groups (analysis of the factors affecting ICE shown in Table S2). Therefore, a thin carbon layer was coated on SiNPs@C_{HD} composite via CVD with acetylene as the precursor. The CVD carbon coating significantly reduced the specific surface area of SiNPs@C_{HD} to 13 m^2 g^{-1} with a slight decrease of the Si content to 44.5 wt % (analyses in Figures S9 and 10). As the scanning electron microscopic (SEM) image shows in Figure 5 a, the carbon coated SiNPs@C_{HD} composite has a flake-like structure composed of fused SiNPs@C_{HD} particles. The SEM image of the cross-section of the graphite–SiNPs@C_{HD} anode (Figure 5 b) shows these two materials are uniformly stacked together with a total thickness of about 50–60 μm. The graphite-SiNPs@C_{HD} anodes demonstrate reversible capacity of 600 mAh g^{-1} (3.1 mg cm^{-2} loading) under a current density of 250 mA g^{-1} and 450 mAh g^{-1} (4.5 mg cm^{-2} loading) under a current density of 500 mA g^{-1}, with corresponding ICEs of 74 % and 72 %. Compared to the specific capacity of 292 mAh g^{-1} obtained from the pure graphite anode with comparable loading (Figure S11), the capacity shows an increase of over 100 % with the addition of the SiNPs@C_{HD} composite. The graphite–SiNPs@C_{HD} anode under 250 mA g^{-1} current density displays excellent capacity retention, demonstrated by the stable lithiation/delithiation voltage profile at various cycles in Figure 5 d.

In summary, we developed unique colloidal routes to synthesize SiNPs@C composite materials. The surface functionalization of the SiNP surface with long alkyl chains renders good solubility in organic solvents, thus enabling oil-in-water emulsions with SiNPs dissolved in the dispersed phase. Sol–gel polymerization of RF resin in the emulsions can encapsulate the dispersed phase containing the SiNPs, from which SiNPs@C composites can be obtained via carbonization. We studied PS (hard template) from in situ polymerization of styrene and HD (soft template) as the dispersed phase in the colloidal synthesis. The results clearly show that the SiNPs@C from the soft template route demonstrates superior performance as the anode material for Li-ion batteries due to the more uniform SiNPs distribution in the composite. As the additive to the conventional graphite anode, this SiNPs@C composite could significantly improve the overall specific capacity with relatively high areal loading of active materials. The promising performance of the SiNPs@C composites are strong evidence that the colloidal synthesis based on soluble SiNPs can be a viable method to produce practical Si–C anode materials for Li-ion batteries. However, the low ICE remains the most significant challenge of the reported SiNPs@C composites, although CVD carbon coating appears a viable approach to reducing the high surface area. Future investigation will focus on optimizing the secondary carbon structure to minimize the surface area, and more emphasis will be put on the design and fabrication of graphite–SiNPs@C composite anodes.

Acknowledgements

H.S. is grateful to the Chinese Scholarship Council for the visiting fellowship. A.A.B. acknowledges the support of the "Consejo Nacional de Ciencia *y* Tecnología" (CONACYT, Mexico) and The University of California Institute for Mexico and the United States (UC MEXUS). L.M. acknowledges the support of the National Science Foundation under

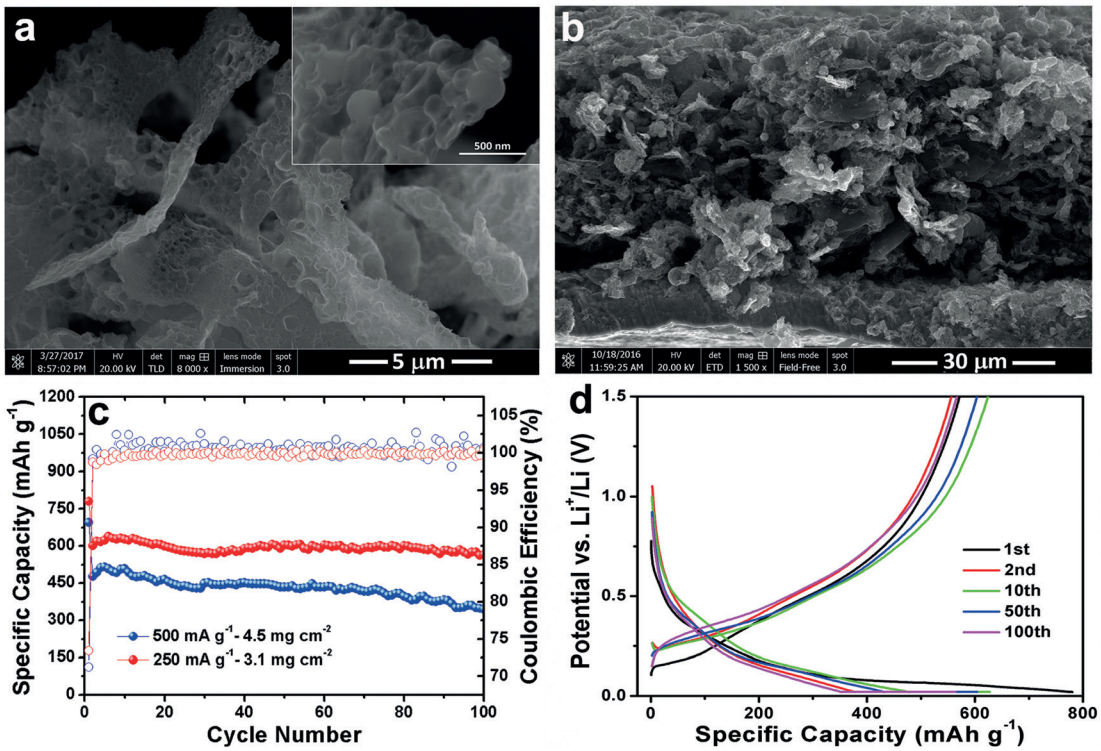

Figure 5. SEM images of a) SiNPs@C_{HD} composite after carbon coating via CVD and b) cross-section of the anode composed of graphite and carbon coated SiNPs@C_{HD}. c) Cycling stability and CE of the graphite-SiNPs@C_{HD} anodes under 250 mA g^{-1} and 500 mA g^{-1}. d) Representative lithiation/delithiation voltage profiles of the graphite–SiNPs@C_{HD} anode at 250 mA g^{-1} vs. Li^+/Li.

award number 1351386 (CAREER). J.G. acknowledges the financial support from University of California, Riverside.

Conflict of interest

The authors declare no conflict of interest.

Keywords: anodes · colloids · composite materials · emulsions · lithium-ion batteries

How to cite: *Angew. Chem. Int. Ed.* **2017**, *56*, 10780–10785
Angew. Chem. **2017**, *129*, 10920–10925

[1] a) B. Liang, Y. Liu, Y. Xu, *J. Power Sources* **2014**, *267*, 469–490; b) M. A. Rahman, G. Song, A. I. Bhatt, Y. C. Wong, C. Wen, *Adv. Funct. Mater.* **2016**, *26*, 647–678; c) X. Su, Q. Wu, J. Li, X. Xiao, A. Lott, W. Lu, B. W. Sheldon, J. Wu, *Adv. Energy Mater.* **2014**, *4*, 1300882; d) X. Zuo, J. Zhu, P. Müller-Buschbaum, Y.-J. Cheng, *Nano Energy* **2017**, *31*, 113–143.

[2] a) J. Yang, Y.-X. Wang, S.-L. Chou, R. Zhang, Y. Xu, J. Fan, W.-X. Zhang, H. Kun Liu, D. Zhao, S. X. Dou, *Nano Energy* **2015**, *18*, 133–142; b) A. Casimir, H. Zhang, O. Ogoke, J. C. Amine, J. Lu, G. Wu, *Nano Energy* **2016**, *27*, 359–376.

[3] a) X. H. Liu, L. Zhong, S. Huang, S. X. Mao, T. Zhu, J. Y. Huang, *ACS Nano* **2012**, *6*, 1522–1531; b) M. Gu, Y. Li, X. Li, S. Hu, X. Zhang, W. Xu, S. Thevuthasan, D. R. Baer, J.-G. Zhang, J. Liu, *ACS Nano* **2012**, *6*, 8439–8447; c) M. T. McDowell, S. W. Lee, C. Wang, W. D. Nix, Y. Cui, *Adv. Mater.* **2012**, *24*, 6034–6041.

[4] a) C. K. Chan, H. Peng, G. Liu, K. McIlwrath, X. F. Zhang, R. A. Huggins, Y. Cui, *Nat. Nanotechnol.* **2008**, *3*, 31–35; b) J. Kong, W. A. Yee, Y. Wei, L. Yang, J. M. Ang, S. L. Phua, S. Y. Wong, R. Zhou, Y. Dong, X. Li, X. Lu, *Nanoscale* **2013**, *5*, 2967–2973; c) D. Lin, Z. Lu, P.-C. Hsu, H. R. Lee, N. Liu, J. Zhao, H. Wang, C. Liu, Y. Cui, *Energy Environ. Sci.* **2015**, *8*, 2371–2376.

[5] a) Y.-X. Yin, S. Xin, L.-J. Wan, C.-J. Li, Y.-G. Guo, *J. Phys. Chem. C* **2011**, *115*, 14148–14154; b) Q. Xu, J. Y. Li, J. K. Sun, Y. X. Yin, L. J. Wan, Y. G. Guo, *Adv. Energy Mater.* **2017**, *7*, 1601481.

[6] a) J. Song, S. Chen, M. Zhou, T. Xu, D. Lv, M. L. Gordin, T. Long, M. Melnyk, D. Wang, *J. Mater. Chem. A* **2014**, *2*, 1257–1262; b) H. Kim, M. Seo, M. H. Park, J. Cho, *Angew. Chem. Int. Ed.* **2010**, *49*, 2146–2149; *Angew. Chem.* **2010**, *122*, 2192–2195; c) N. Liu, Z. Lu, J. Zhao, M. T. McDowell, H.-W. Lee, W. Zhao, Y. Cui, *Nat. Nanotechnol.* **2014**, *9*, 187–192.

[7] a) G. Hou, B. Cheng, Y. Cao, M. Yao, B. Li, C. Zhang, Q. Weng, X. Wang, Y. Bando, D. Golberg, F. Yuan, *Nano Energy* **2016**, *24*, 111–120; b) K. Feng, W. Ahn, G. Lui, H. W. Park, A. G. Kashkooli, G. Jiang, X. Wang, X. Xiao, Z. Chen, *Nano Energy* **2016**, *19*, 187–197; c) Z. Lu, N. Liu, H.-W. Lee, J. Zhao, W. Li, Y. Li, Y. Cui, *ACS Nano* **2015**, *9*, 2540–2547.

[8] L. Zhang, R. Rajagopalan, H. Guo, X. Hu, S. Dou, H. Liu, *Adv. Funct. Mater.* **2016**, *26*, 440–446.

[9] a) Z. Luo, Q. Xiao, G. Lei, Z. Li, C. Tang, *Carbon* **2016**, *98*, 373–380; b) J. Wu, X. Qin, H. Zhang, Y.-B. He, B. Li, L. Ke, W. Lv, H. Du, Q.-H. Yang, F. Kang, *Carbon* **2015**, *84*, 434–443.

[10] a) J. K. Yoo, J. Kim, Y. S. Jung, K. Kang, *Adv. Mater.* **2012**, *24*, 5452–5456; b) T. H. Hwang, Y. M. Lee, B.-S. Kong, J.-S. Seo, J. W. Choi, *Nano Lett.* **2012**, *12*, 802–807; c) J. Chang, X. Huang, G. Zhou, S. Cui, P. B. Hallac, J. Jiang, P. T. Hurley, J. Chen, *Adv. Mater.* **2014**, *26*, 758–764; d) P. Wu, H. Wang, Y. Tang, Y. Zhou, T. Lu, *ACS Appl. Mater. Interfaces* **2014**, *6*, 3546–3552; e) Y. Li, K. Yan, H.-W. Lee, Z. Lu, N. Liu, Y. Cui, *Nat. Energy* **2016**, *1*, 15029; f) M. Ko, S. Chae, S. Jeong, P. Oh, J. Cho, *ACS Nano* **2014**, *8*, 8591–8599; g) S. Suresh, Z. P. Wu, S. F. Bartolucci, S. Basu, R. Mukherjee, T. Gupta, P. Hundekar, Y. Shi, T.-M. Lu, N. Koratkar, *ACS Nano* **2017**, *11*, 5051–5061.

[11] a) A. Magasinski, P. Dixon, B. Hertzberg, A. Kvit, J. Ayala, G. Yushin, *Nat. Mater.* **2010**, *9*, 353 – 358; b) M. Li, X. Hou, Y. Sha, J. Wang, S. Hu, X. Liu, Z. Shao, *J. Power Sources* **2014**, *248*, 721 – 728; c) B. Wang, X. Li, X. Zhang, B. Luo, M. Jin, M. Liang, S. A. Dayeh, S. Picraux, L. Zhi, *ACS Nano* **2013**, *7*, 1437 – 1445.

[12] L. Mangolini, E. Thimsen, U. Kortshagen, *Nano Lett.* **2005**, *5*, 655 – 659.

[13] C. Li, T. Shi, D. Li, H. Yoshitake, H. Wang, *RSC Adv.* **2016**, *6*, 34715 – 34723.

[14] a) B. Fuchsbichler, C. Stangl, H. Kren, F. Uhlig, S. Koller, *J. Power Sources* **2011**, *196*, 2889 – 2892; b) C. Martin, M. Alias, F. Christien, O. Crosnier, D. Bélanger, T. Brousse, *Adv. Mater.* **2009**, *21*, 4735 – 4741; c) S. W. Kim, J. H. Yun, B. Son, Y. G. Lee, K. M. Kim, Y. M. Lee, K. Y. Cho, *Adv. Mater.* **2014**, *26*, 2977 – 2982.

[15] a) Y.-C. Yen, S.-C. Chao, H.-C. Wu, N.-L. Wu, *J. Electrochem. Soc.* **2009**, *156*, A95 – A102; b) J. Ryu, D. Hong, M. Shin, S. Park, *ACS Nano* **2016**, *10*, 10589 – 10597; c) C. Wang, F. Luo, H. Lu, X. Rong, B. Liu, G. Chu, Y, Sun, B. Quan, J. Zheng, J. Li, C. Gu, X. Qiu, H. Li, L. Chen, *ACS Appl. Mater. Interfaces* **2017**, *9*, 2806 – 2814.

Manuscript received: May 19, 2017
Revised manuscript received: July 9, 2017
Accepted manuscript online: July 14, 2017
Version of record online: July 31, 2017

Angewandte Chemie
Eine Zeitschrift der Gesellschaft Deutscher Chemiker

Supporting Information

Colloidal Synthesis of Silicon–Carbon Composite Material for Lithium-Ion Batteries

Haiping Su, Alejandro A. Barragan, Linxiao Geng, Donghui Long, Licheng Ling, Krassimir N. Bozhilov, Lorenzo Mangolini, and Juchen Guo**

ange_201705200_sm_miscellaneous_information.pdf

SUPPORTING INFORMATION

Experimental Procedures

Synthesis of SiNPs and surface functionalization: The SiNPs were synthesized using a radio-frequency induced non-thermal plasma technique, and the dodecyl chains were grafted onto the surface of SiNPs via a reflux reaction[1]. In brief, 300 mg SiNPs were transferred to a round-bottom flask within an argon-filled glove box and then dispersed in a solution of 1-dodecane in mesitylene (1:4 volume ratio) under ultrasonication for 15 min. The grafting reaction took place through a reflux process with argon protection at 165 °C for 4 h till the color of the solution changed to a translucent dark brown. After that, the surface functionalized particles $C_{12}H_{25}$-SiNPs were collected by rotary evaporation.

Synthesis of the SiNPs@C_{PS} composite (hard-template route): In a typical experiment, 200 mg of the $C_{12}H_{25}$-SiNPs, 200 μL HD and 0.011 g azobisisobutyronitrile (AIBN) were co-dissolved in 1 mL styrene. The solution was then mixed into a 30 mL H_2O solution of 1 mM hexadecyltrimethylammonium bromide (CTAB) with probe sonication to form a stable emulsion. The emulsion was heated at 60 °C to initiate the free radial polymerization of polystyrene under agitation. The reaction was kept at 60 °C for 8 h to obtain the colloid containing SiNPs@PS Janus particles. To coat RF on SiNPs@PS, the as-prepared SiNPs@PS dispersion was diluted by adding 30 mL water, after which it was mixed with 0.1 mL ammonium hydroxide (28 wt.% NH_3 in H_2O), 0.2 g resorcinol, and 0.28 mL formaldehyde solution (37 wt.% in H_2O). The mixture was further stirred for 16 hours at room temperature[2]. The SiNPs@PS@RF was extracted from the colloid via freeze-drying and was heated at 800 °C for 3 h in argon to produce the SiNPs@C_{PS} composite.

Synthesis of the SiNPs@C_{HD} composite (soft-template route): In a typical experiment, 200 mg $C_{12}H_{25}$-SiNPs was first dissolved in 600 μL HD. The obtained HD solution was dispersed in a 30 mL water solution of 1 mM CTAB with sonication to form a uniform oil-in-water emulsion. 0.1 mL ammonium hydroxide (28 wt.% NH_3 in H_2O), 0.05 g resorcinol, and 0.07 mL formaldehyde (37 wt.% in H_2O) were dissolved into the obtained emulsion to coat the SiNPs-in-HD droplets with RF[2]. The mixture was stirred for 16 hours at room temperature. The final product was collected via freeze-drying and carbonized at 800 °C for 3 h in argon to produce the SiNPs@C_{HD} composite.

Carbon coating SiNPs@C_{HD} composite via CVD: CVD carbon coating was performed by flowing acetylene gas at 15 sccm through a 1-inch diameter, 20-inch long quartz reactor. The system was heated up to 650 °C and held at a pressure of ~380 Torr for 15 min. After that, the reactor was naturally cooled down to room temperature, and the chamber was refilled with pure argon in order to remove the sample without abruptly pressurizing the chamber.

Characterizations: The morphology and microstructures of the SiNPs@C composites and electrodes were characterized with scanning electron microscopy (Nova NanoSEM 450) and transmission electron microscopy (Tecnai 12 and Titan Themis 300 STEM). The crystallinity of the SiNPs in the obtained SiNPs@C composites were analyzed using X-ray diffraction (XRD, PANalytical EMPYREAN) with a CuKα source (Figure S12 in Supporting Information). TGA was conducted with a TA Instrument analyzer (Q 500) at a heating rate of 10 °C min^{-1} from room temperature to 800 °C in dry air with a one-hour isothermal step at 800 °C. N_2 adsorption-desorption was performed with an ASAP 2020 instrument. The specific surface area was calculated using the Brunauer-Emmett-Teller (BET) method.

Electrochemical Measurements: The SiNPs@C anode slurry was prepared by mixing the SiNPs@C composites, acetylene black, and CMC binder in a weight ratio of 85: 10: 5 in deionized water. The homogeneous slurry was pasted onto the carbon-coated copper foil and then vacuum dried at 110 °C overnight. The SiNPs@C composite load was approximately 1.0 mg cm^{-2}. Lithium foil was used as the counter electrode and a Celgard 2400 membrane was used as the separator. The electrolyte was 1.0 M $LiPF_6$ in ethylene carbonate/diethyl carbonate (1:1 volume ratio). The 2032 coin cells were assembled in an argon-filled glove box. The electrochemical lithiation-delithiation were carried on an Arbin battery test station, and CV was conducted on a Gamry Interface 1000 with a scan rate of 0.1 mV s^{-1}. To prepare the graphite-SiNPs@C_{HD} anodes, aqueous slurry consisting of carbon-coated SiNPs@C_{HD} composite, graphite (artificial graphite powder from MTI Inc.), acetylene black, and carboxymethyl cellulose binder with weight ratio of 46: 46: 5: 3 was pasted onto the copper current collector and then dried in a vacuum oven at 110 °C overnight. The mass loading of active materials (graphite+SiNPs@C_{HD}) was > 3.0 mg cm^{-2}. The cycling performance of the anodes was evaluated using a protocol with constant-current-constant-voltage (CCCV) lithiation (charging in full battery) and constant-current delithiation (discharging in full battery). The CCCV lithiation was used to overcome the lithiation potential difference between graphite and Si; a constant current was applied until the potential dropped to 0.02 V vs. the Li counter electrode, and the potential was subsequently maintained at 0.02 V for 3 h.

[1] a) L. Mangolini, E. Thimsen, U. Kortshagen, *Nano letters* **2005**, *5*, 655-659; b) L. Zhong, J. Guo, L. Mangolini, *Journal of Power Sources* **2015**, *273*, 638-644.
[2] N. Li, Q. Zhang, J. Liu, J. Joo, A. Lee, Y. Gan, Y. Yin, *Chem Commun (Camb)* **2013**, *49*, 5135-5137.

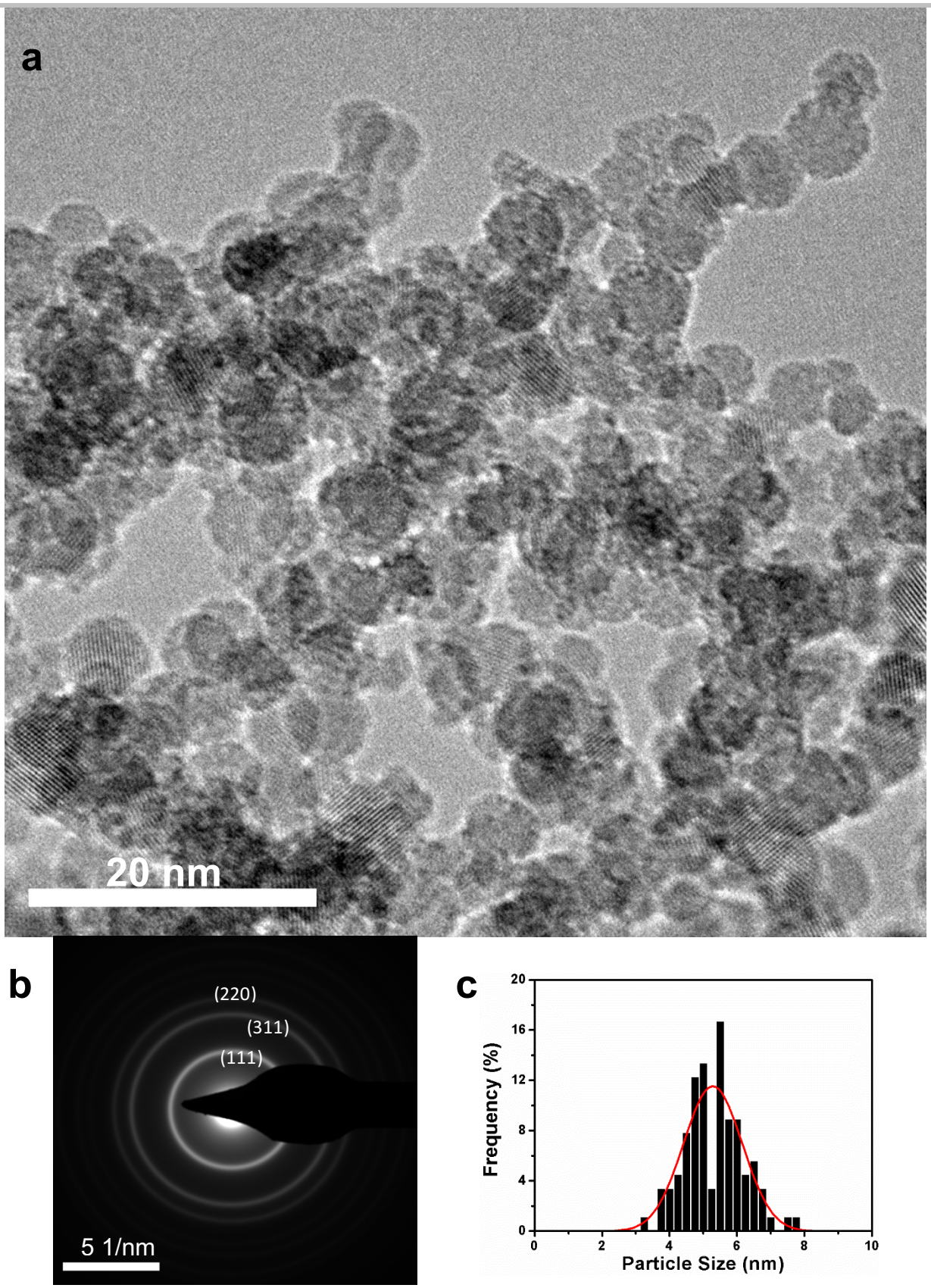

Figure S1. (a) High-magnification bright field TEM micrograph of the pristine SiNPs synthesized with the non-thermal plasma method, the lattice fringes from the crystallites can be clearly observed; (b) Selected area electron diffraction pattern of the pristine SiNPs from lower magnification TEM with several hundred of SiNPs in the formation of the diffraction pattern, polycrystalline ring including (111), (311) and (220) can be identified, which is contestant with the power XRD pattern in Figure S12; and (c) SiNPs particle size histogram extracted from total 10 high-magnification TEM micrographs, the mean of the particle size distribution is 5.25 nm based on a Gaussian distribution.

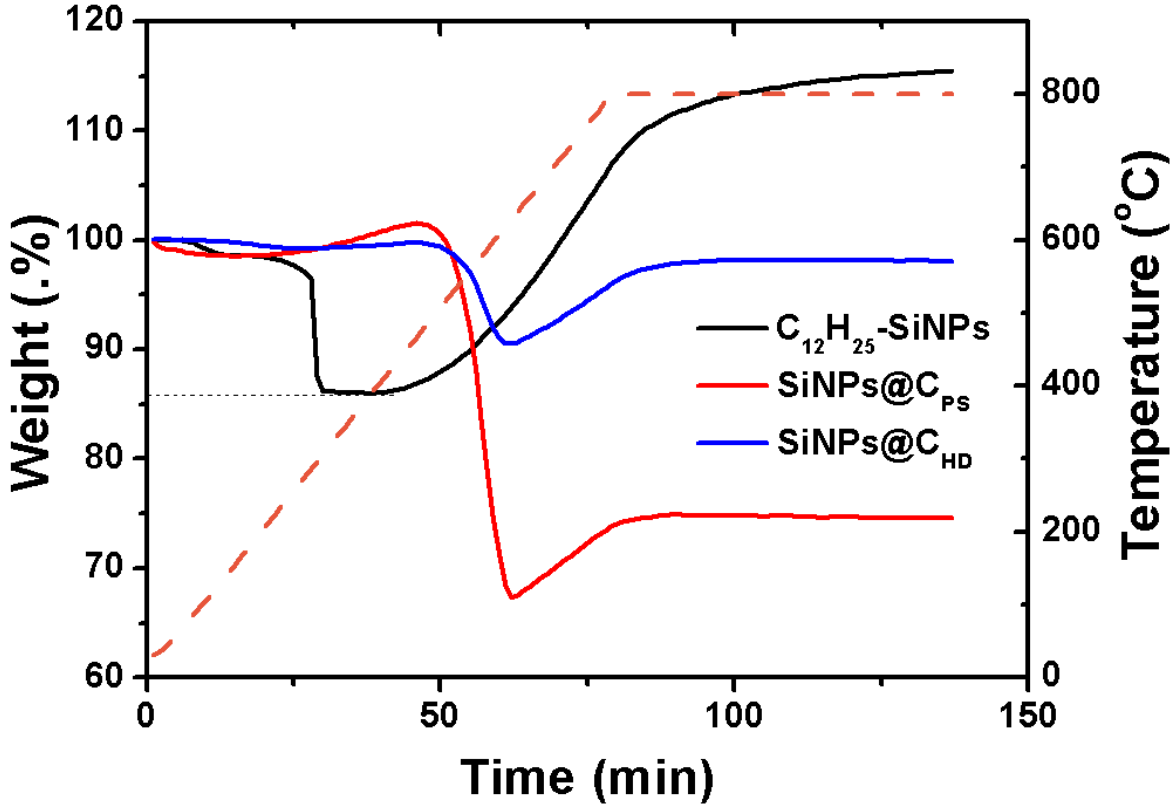

Figure S2. TGA of $C_{12}H_{25}$-SiNPs (black), SiNPs@C_{PS} (red), and SiNP@C_{HD} (blue) in dry air. The Si content of $C_{12}H_{25}$-SiNPs was measured to be 86.5 wt.%, considering that the surface alkyl chain entirely decomposed at around 400 °C. The SiNPs@C composites were assumed to be fully oxidized to SiO_2 after total removal of the carbon content in air at 800 °C. The Si content of SiNPs@C_{PS} and SiNP@C_{HD} were calculated to be 35 wt.% and 46 wt.%, respectively, as described below:

Assuming the mass of Si in SiNPs@C is *x* and the mass of C is *y* out of 100, therefore $x + y = 100$ (i.e. 100% weight at the beginning of the TGA). After full carbon removal and oxidization to SiO_2 in dry air: $(60/28)x = 75$ for SiNPs@C_{PS}, and $(60/28)x = 98.6$ for SiNPs@C_{HD} from TGA (28 represents the atomic weight of Si, and 60 represents the formula weight of SiO_2). Therefore, it can be calculated $x = 35$ for SiNPs@C_{PS} and $x = 46$ for SiNPs@C_{HD}.

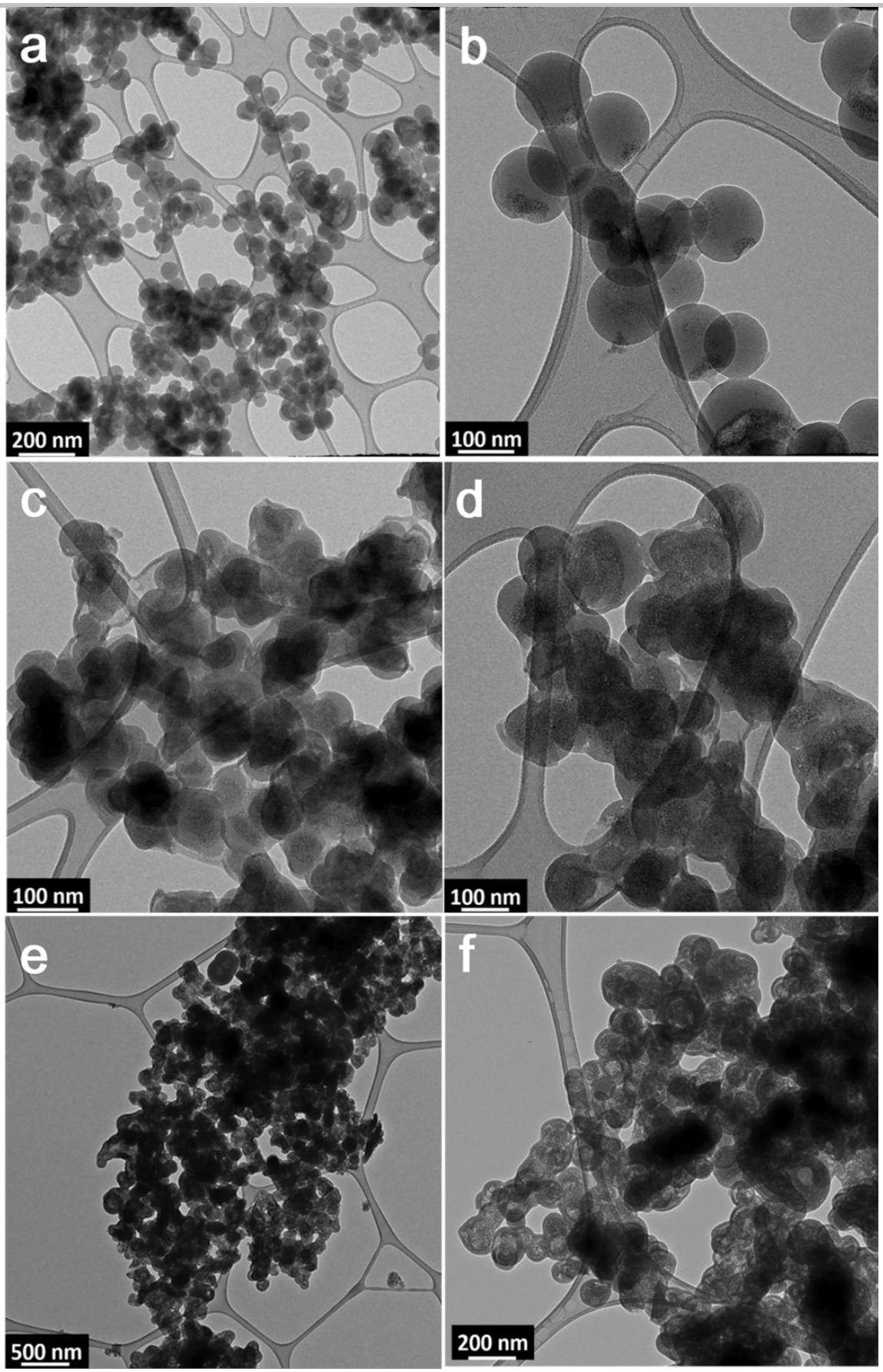

Figure S3. TEM images of (a, b) SiNPs@PS, (c, d) RF coated SiNPs@PS and (e, f) SiNPs@C_{PS} at different magnifications.

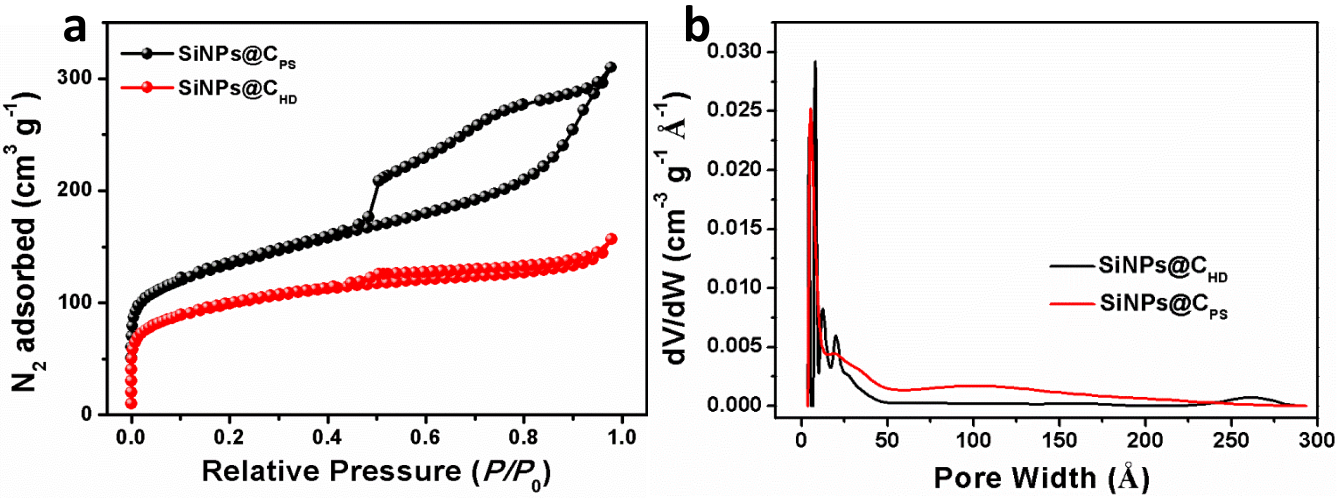

Figure S4. (a) N_2 adsorption-desorption isotherms of SiNPs@C_{PS} (black) and SiNPs@C_{HD} (red). Both SiNPs@C_{PS} and SiNPs@C_{HD} composites show type-IV curves, demonstrating the presence of mesopores. The H2 hysteresis of the SiNPs@C_{PS} composite indicates the particle-packing structure, while the H4 hysteresis of SiNPs@C_{HD} composite indicates the layer structure; (b) the pore size distribution of SiNPs@C_{PS} and SiNPs@C_{HD}.

Table S1. Calculated BET specific surface area and pore volume of SiNPs@C_{PS} and SiNPs@C_{HD}.

	S_{BET} (m^2 g^{-1})	V_t (cm^3 g^{-1})
SiNPs@C_{PS}	437	0.45
SiNPs@C_{HD}	317	0.23

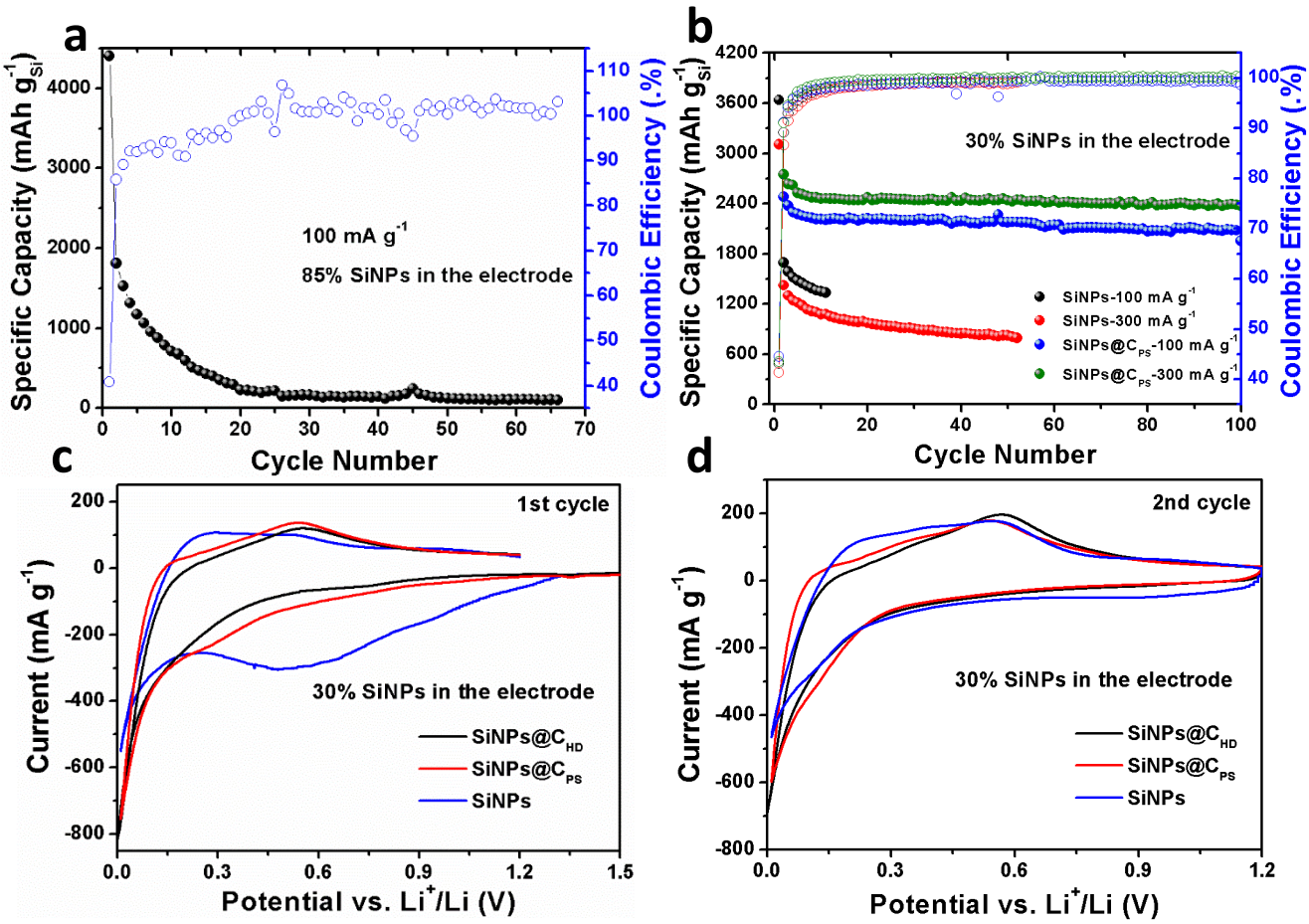

Figure S5. Cycle stability and CE of electrodes composed of (a) 85 wt.% of pure SiNPs at 100 mAh g^{-1} and (b) 30 wt.% of pure SiNPs, 60 wt.% of carbon black and 10 wt.% of CMC binder in comparison with the performance of electrodes composed of SiNPs@C_{PS}, which also has 30 wt.% of SiNPs in total. It is clear that the cycle stability of the electrode composed of SiNPs@C_{PS} is significantly improved due to the superior microstructure of SiNPs@C_{PS}; (c, d) The comparison of the 1st-cycle and 2nd-cycle CV (0.1 mV s^{-1}) curves of electrodes with pure SiNPs with 30 wt.% SiNPs, SiNPs@C_{PS} and SiNPs@C_{HD}. The 1st-cycle CV curve of the pure SiNPs shows a broad lithiation peak at 0.5 V vs Li^+/Li, which is believed due to the irreversible Li-ion adsorption (and SEI formation) on the carbon black additives and SEI formation. On the contrary, such behavior is not observed in the SiNPs@C composites. However, the CV curve of SiNPs@C_{PS} electrode does indicate more SEI formation by the higher cathodic current density in the potential range between 0.7 and 0.2 V. The comparison of the 2nd-cycle CV curves indicates the similar electrochemical behaviors of all three electrodes, although the pure SiNPs electrode may have higher Li-ion adsorption-desorption mechanism indicated by the delithiation peak at low potential of 0.15 V vs. Li^+/Li, which was consistent with its 1st-cycle CV cycle in (c).

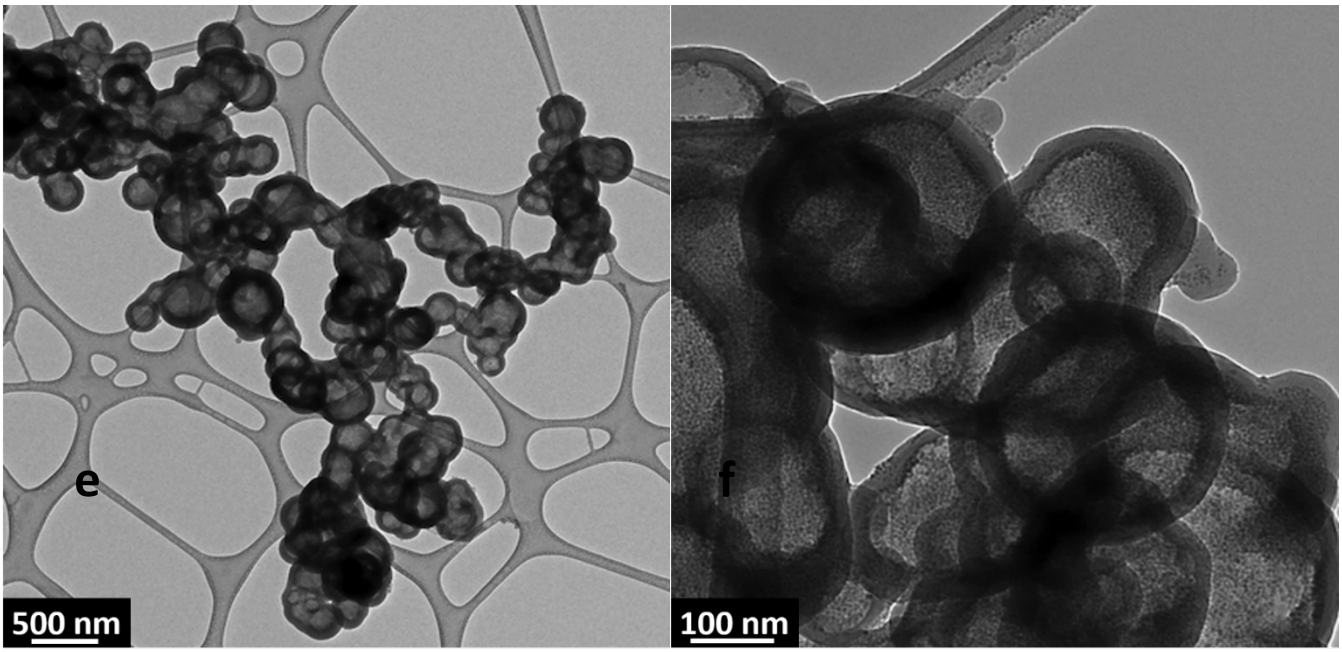

Figure S6. (a) TEM image and (b) high-magnification TEM image of the SiNPs@RF particles before carbonization.

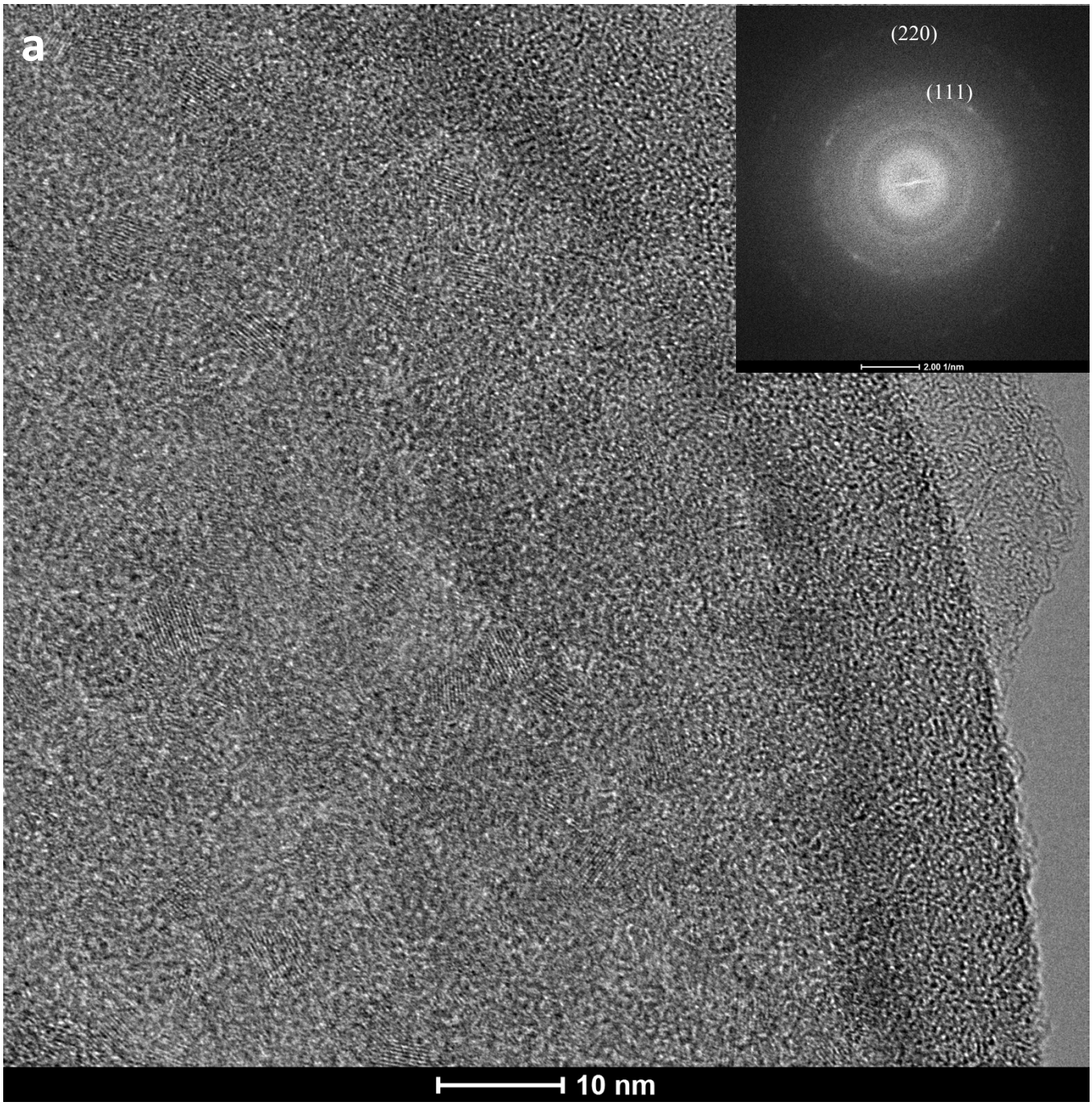
a
(220)
(111)
2.00 1/nm
10 nm

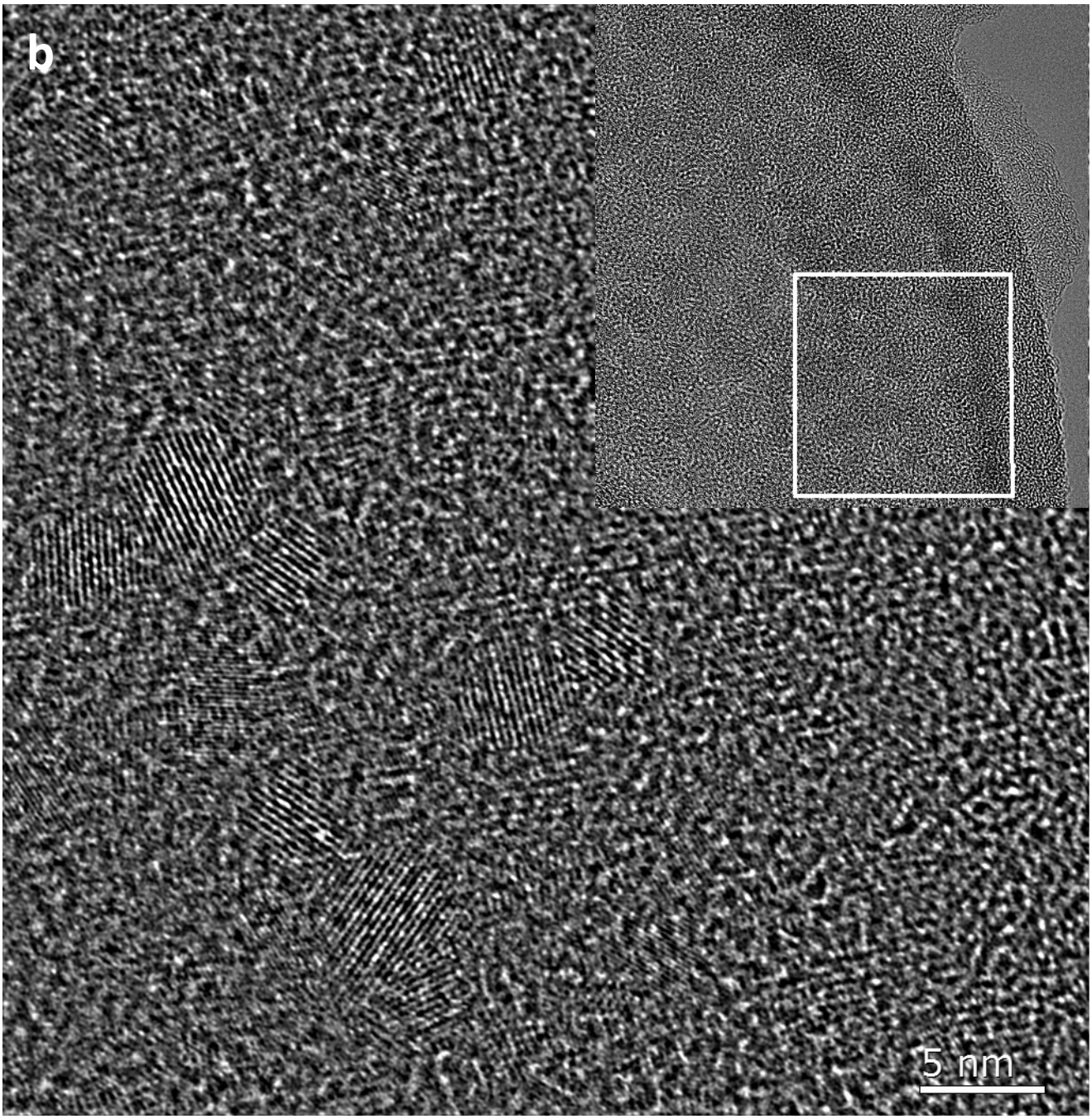

Figure S7. (a) High-magnification TEM image of a SiNPs@C_{HD} particle with selected area electron diffraction showing the polycrystalline ring; and (b) enlargement of a portion of the TEM image in (a) (as the frame shown in the inset) clearly showing the lattice fringes from the crystallites around 5 nm, which is consistent with the pristine SiNPs shown in Figure S1.

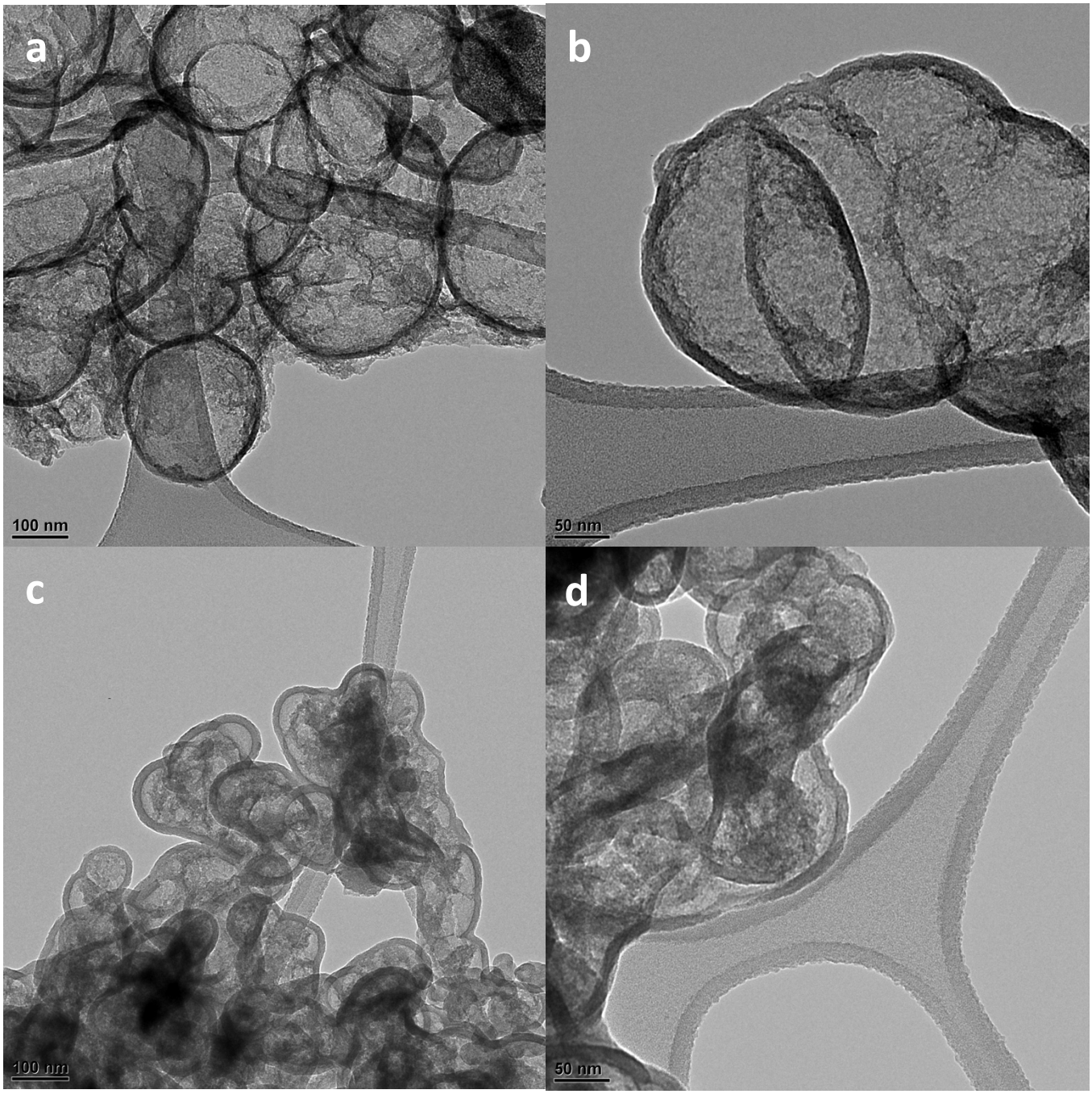

Figure S8. TEM image of (a, b) SiNPs@C_{HD} and (c, d) SiNPs@C_{PS} after 200 cycles at 1/3 C. Despite the fact that SiNPs become amorphous, the microstructures of the SiNPs@C composites are intact after prolonged cycling.

SUPPORTING INFORMATION

Table S2. Comparison of the initial coulombic efficiency (ICE) and the affecting parameters in recent literature to this work.

Ref	Si-C Composite	Carbon source	Carbon formation method	Carbon wt.%	S_{BET} $m^2 g^{-1}$	OCP prior to 1st lithiation / V	ICE
1	Yolk-Shell Si@C	Phenolic resin	Carbonization	57.8	582	> 2.4	~ 46%
	Yolk-Shell Si@C	Phenolic resin	Carbonization	26.6	362	--	~ 62%
2	Si NP-carbon fiber	Commercial carbon fiber	--	53.7	--	1.7	~ 50%
3	Carbon coated hollow Si spheres	dopamine	Carbonization	30	253	1.7	52.4%
4	Si@SiOx/C nano-composite	glucose	Carbonization	26	--	2.7	~ 55%
5	Mesoporous silicon sponge/C	acetylene	CVD	34	155.8	2.0	56%
6	Si-C core shell cluster	Resorcinol-formaldehyde	Carbonization	27	--	1.8	~ 59%
	Si-C core shell cluster	Resorcinol-formaldehyde	Carbonization	17	--	1.8	~ 70%
	Si-C core shell cluster	Resorcinol-formaldehyde	Carbonization	6	--	1.8	~ 77%
7	Si/C nanoporous microspheres	PVP	Carbonization	24	57	2.7	65%
8	pSiMP impregnation coating	Resorcinol-formaldehyde	Carbonization	21	--	--	68%
	pSiMP non-filling coating	Resorcinol-formaldehyde	Carbonization	11	--	--	78%
9	Si/rGO	Reduced GO	--	26.1	--	2.0	~ 68%
	Si/rGO-CVD	rGO/toluene	CVD	21.3	--	1.6	75%
10	Nano Si@C	Phenolic resin	Carbonization	21	41.3	2.7	~ 74%
11	Pomegranae-like Si/C spheres	Resorcinol-formaldehyde	Carbonization	23	--	< 1.0	75%
	Pomegranae-like Si/C spheres	Resorcinol-formaldehyde	Carbonization	9	--	< 1.0	82%
12	Si-C composite	acetylene	CVD	20	313	1.9	77%
13	Si-C granules	C3H6	CVD	50	24	1.5	85%
14	Plum-pudding-like Si/C composite	glucose	Carbonization	6.3	74	< 1.5	88%
15	Watermelon-inspired Si/C microspheres	acetylene	CVD	12.5	9.7	1.2	89.2%
This Work	SiNPs@C_{HD}	Resorcinol-formaldehyde	Carbonization	54	317	2.7	49%
	SiNPs@C_{HD} – CVD	acetylene	CVD	55.5	13	1.4	74%

[1] J. Yang, Y.-X. Wang, S.-L. Chou, R. Zhang, Y. Xu, J. Fan, W.-x. Zhang, H. K. Liu, D. Zhao, S. X. Dou, *Nano Energy* **2015**, *18*, 133-142.
[2] Y. Xu, E. Swaans, S. Chen, S. Basak, P.-P. R. Harks, B. Peng, H. W. Zandbergen, D. M. Borsa, F. M. Mulder, *Nano Energy* **2017**.
[3] S. Fang, Z. Tong, P. Nie, G. Liu, X. Zhang, *ACS applied materials & interfaces* **2017**.
[4] Y. S. Hu, R. Demir-Cakan, M. M. Titirici, J. O. Müller, R. Schlögl, M. Antonietti, J. Maier, *Angewandte Chemie International Edition* **2008**, *47*, 1645-1649.
[5] X. Li, M. Gu, S. Hu, R. Kennard, P. Yan, X. Chen, C. Wang, M. J. Sailor, J.-G. Zhang, J. Liu, *Nature communications* **2014**, *5*.
[6] D. Lin, Z. Lu, P.-C. Hsu, H. R. Lee, N. Liu, J. Zhao, H. Wang, C. Liu, Y. Cui, *Energy & Environmental Science* **2015**, *8*, 2371-2376.
[7] Y.-X. Yin, S. Xin, L.-J. Wan, C.-J. Li, Y.-G. Guo, *The Journal of Physical Chemistry C* **2011**, *115*, 14148-14154.
[8] Z. Lu, N. Liu, H.-W. Lee, J. Zhao, W. Li, Y. Li, Y. Cui, *ACS nano* **2015**, *9*, 2540-2547.
[9] K. Feng, W. Ahn, G. Lui, H. W. Park, A. G. Kashkooli, G. Jiang, X. Wang, X. Xiao, Z. Chen, *Nano Energy* **2016**, *19*, 187-197.
[10] Z. Liu, X. Chang, T. Wang, W. Li, H. Ju, X. Zheng, X. Wu, C. Wang, J. Zheng, X. Li, *ACS nano* **2017**.
[11] N. Liu, Z. Lu, J. Zhao, M. T. McDowell, H.-W. Lee, W. Zhao, Y. Cui, *Nature nanotechnology* **2014**, *9*, 187-192.
[12] R. Yi, F. Dai, M. L. Gordin, H. Sohn, D. Wang, *Advanced Energy Materials* **2013**, *3*, 1507-1515.
[13] A. Magasinski, P. Dixon, B. Hertzberg, A. Kvit, J. Ayala, G. Yushin, *Nature materials* **2010**, *9*, 353-358.
[14] G. Hou, B. Cheng, Y. Cao, M. Yao, B. Li, C. Zhang, Q. Weng, X. Wang, Y. Bando, D. Golberg, *Nano Energy* **2016**, *24*, 111-120.
[15] Q. Xu, J. Y. Li, J. K. Sun, Y. X. Yin, L. J. Wan, Y. G. Guo, *Advanced Energy Materials* **2017**, *7*.

From Table S2, the ICE of silicon-carbon anodes is apparently correlated to three parameters: (1) the precursor/method of carbon formation, (2) surface area of the carbon, and (3) the open circuit potential (OCP) of the anodes prior to the first lithiation. It is very clear that Si-C anodes with oxygen-containing hydrocarbon and polymeric precursors have low ICE; On the other hand, the Si-C anodes with carbon coating via CVD universally show high ICE regardless the surface area. However, when the carbon is formed via carbonization of hydrocarbon or polymeric precursors, the ICE is closely related to the surface area of the carbon: the ICE generally decreases with increasing surface area (and/or carbon content). The last observation is that ICE is generally low when the OCP is low regardless the other parameters. It is understandable that lower OCP could avoid irreversible Li-ion adsorption (and SEI formation) on carbon occurring at relatively high potential, thus improving ICE. The cause of the variation of OCP in different studies is not clear, and there has no study focusing on this issue to date.

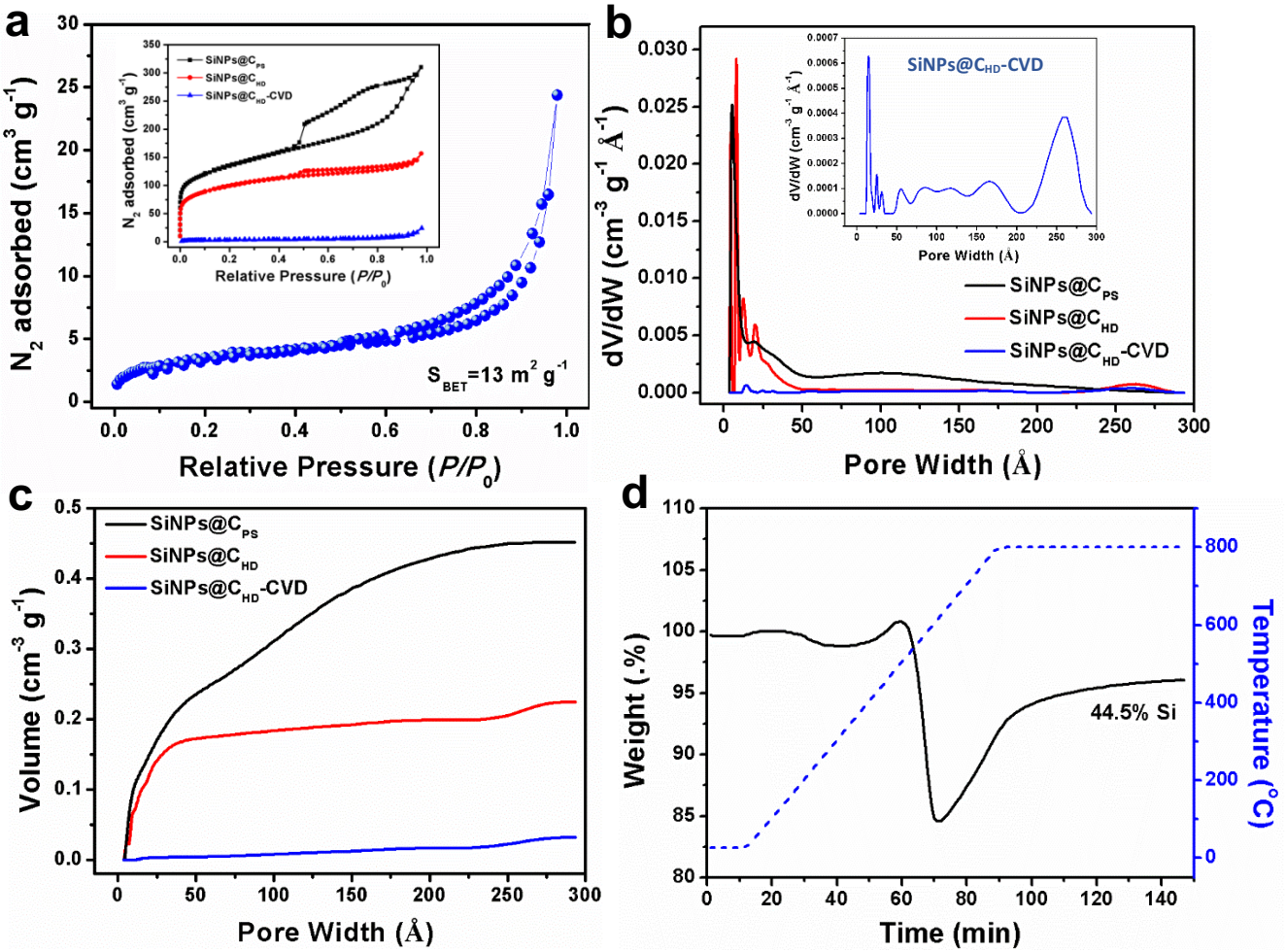

Figure S9. (a) N_2 adsorption-desorption isotherms of the carbon coated SiNPs@C_{HD} via CVD. Inset shows the comparison of the isotherms of SiNPs@C_{PS}, SiNPs@C_{HD} and SiNPs@C_{HD}-CVD. The N_2 adsorption of SiNPs@C_{HD}-CVD was significantly lower than the un-coated ones. The BET surface area is significantly reduced to 13 m^2 g^{-1}, and the reduction of surface area can be explained by figure (b) the pore size distribution of these composites (inset is pore size distribution of SiNPs@C_{HD}-CVD): it is clear that the micropores with width less than 2 nm was drastically reduced by the CVD carbon coating. Figure (c) shows the specific pore volume of SiNPs@C_{HD}-CVD was also significantly reduced by the CVD carbon coating. (d) From TGA the Si content of SiNPs@C_{HD}-CVD was calculated to be 44.5 wt.%, with a slight decrease compared to that of the un-coated SiNPs@C_{HD} (46 wt.%).

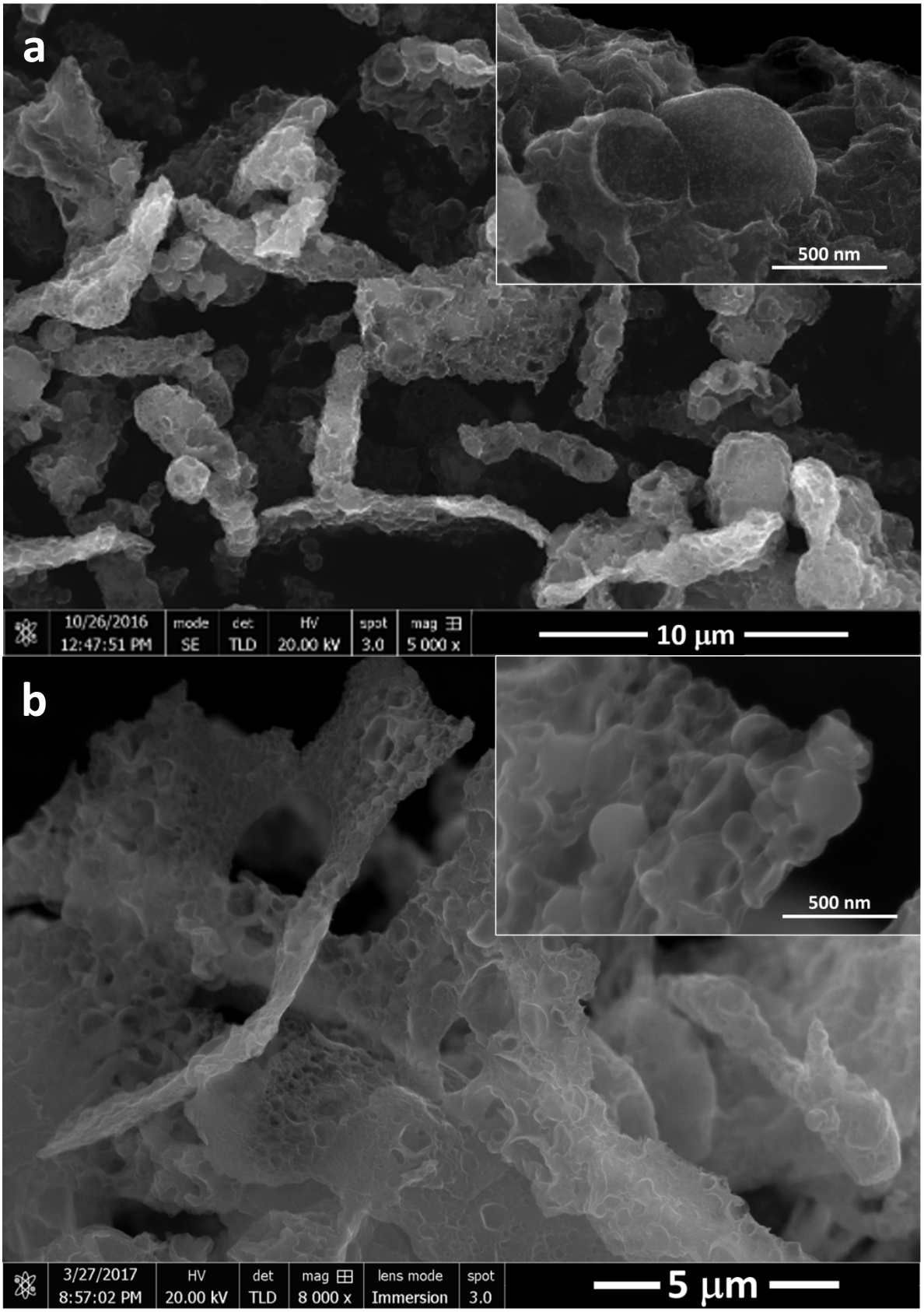

Figure S10. SEM images of (a) SiNPs@C_{HD} and (b) SiNPs@C_{HD}-CVD. The inset image with higher magnification of SiNPs@C_{HD} in (a) shows that SiNPs can be observed on the particle surface. The SEM image of SiNPs@C_{HD}-CVD suggests the overall microstructure does not change after CVD carbon coating. However, the inset with higher magnification of SiNPs@C_{HD}-CVD in (b) shows smooth surface of the composite without observation of SiNPs, indicating uniform CVD carbon coating.

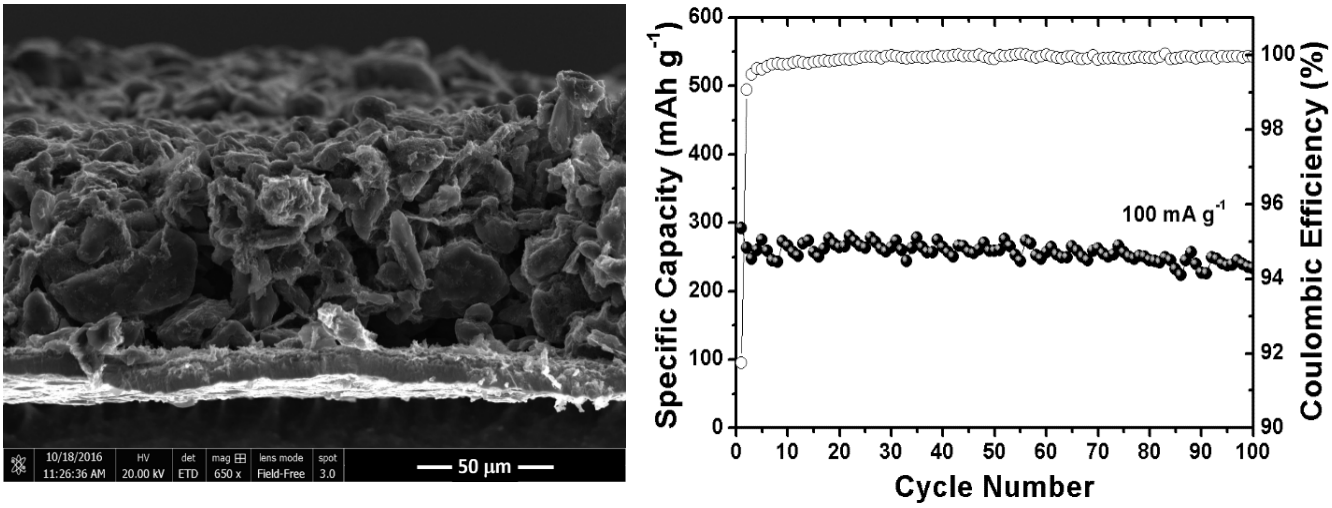

Figure S11. (a) SEM image of the cross-section of the graphite anode, (b) cycle stability of the graphite anode under 100 mA g^{-1} current density.

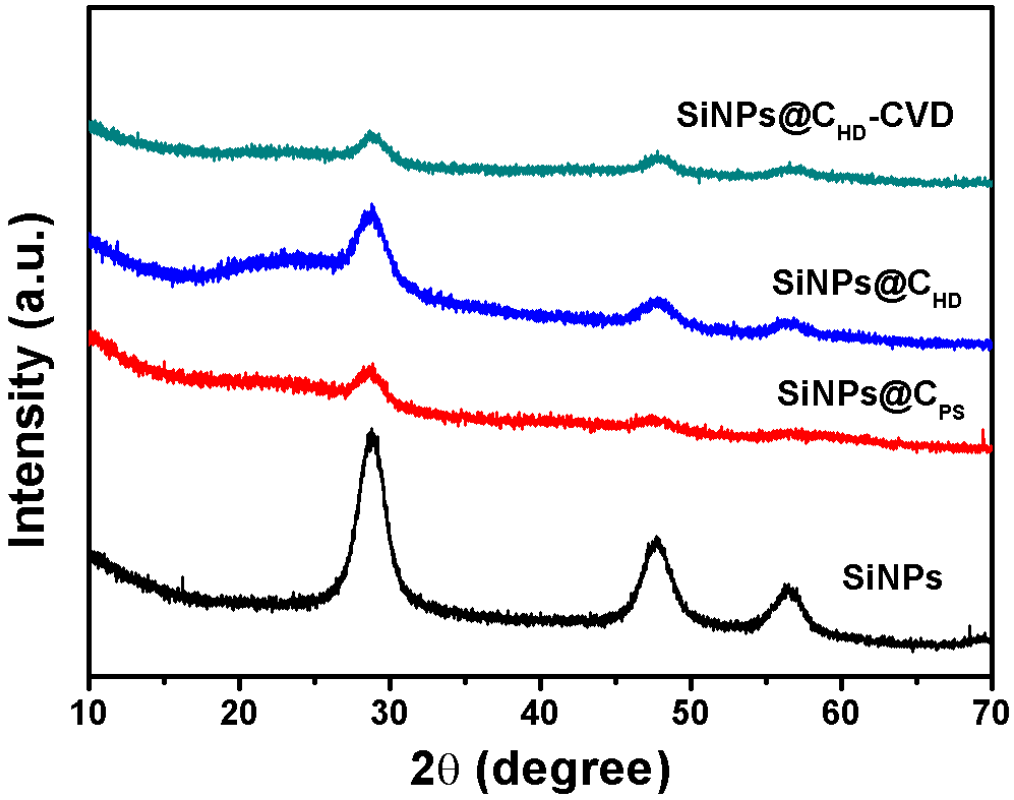

Figure S12. XRD patterns of the pristine SiNPs, SiNPs@C_{PS}, SiNPs@C_{HD}, and carbon coated SiNPs@C_{HD} via CVD. The XRD patterns of all materials clearly show peaks from (111), (220) and (311) crystallographic plans at 28.5°, 47.4° and 56.2°.